

# PCCP

Accepted Manuscript



This is an *Accepted Manuscript*, which has been through the Royal Society of Chemistry peer review process and has been accepted for publication.

*Accepted Manuscripts* are published online shortly after acceptance, before technical editing, formatting and proof reading. Using this free service, authors can make their results available to the community, in citable form, before we publish the edited article. We will replace this *Accepted Manuscript* with the edited and formatted *Advance Article* as soon as it is available.

You can find more information about *Accepted Manuscripts* in the [Information for Authors](#).

Please note that technical editing may introduce minor changes to the text and/or graphics, which may alter content. The journal's standard [Terms & Conditions](#) and the [Ethical guidelines](#) still apply. In no event shall the Royal Society of Chemistry be held responsible for any errors or omissions in this *Accepted Manuscript* or any consequences arising from the use of any information it contains.

# Methane Partial Oxidation using $\text{FeO}_x@ \text{La}_{0.8}\text{Sr}_{0.2}\text{FeO}_{3-\delta}$ Core-Shell Catalyst - Transient Pulse Studies

*Arya Shafiefarhood, Joseph Clay Hamill, Luke Michael Neal, Fanxing Li\**

*\*Department of Chemical and Biomolecular Engineering, North Carolina State University, 911 Partners Way, Raleigh, NC 27695-7905, USA.*

*\*Corresponding author email: fli5@ncsu.edu*

# Methane Partial Oxidation via a Cyclic Redox Scheme - Transient Pulse Studies

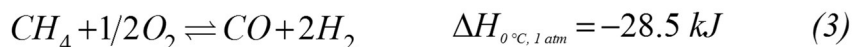
## Abstract

The chemical looping reforming (CLR) process, which utilizes a transition metal oxide based redox catalyst to partially oxidize methane to syngas, represents a potentially efficient approach for methane valorization. The CLR process inherently avoids costly cryogenic air separation by replacing gaseous oxygen with regenerable ionic oxygen ( $O^{2-}$ ) from the catalyst lattice. Our recent studies show that an  $Fe_2O_3@La_{0.8}Sr_{0.2}FeO_{3-\delta}$  core-shell redox catalyst is effective for CLR, as it combines the selectivity of an LSF shell with the oxygen capacity of an iron oxide core. The reaction between methane and the catalyst is also found to be highly dynamic, resulting from changes in lattice oxygen availability and surface properties. In this study, a transient pulse injection approach is used to investigate the mechanisms of methane partial oxidation over the  $Fe_2O_3@LSF$  redox catalyst. As confirmed by isotope exchange, the catalyst undergoes transitions between reaction “regions” with markedly different mechanisms. While oxygen evolution maintains a modified Mars-van Krevlen mechanism throughout the reaction with  $O^{2-}$  conduction being the rate limiting step, the mechanism of methane conversion changes from an Eley-Rideal type in the first reaction region to a Langmuir-Hinshelwood-like mechanism in the third region. Availability of surface oxygen controls the reduction scheme of the catalyst and the underlying reaction mechanism.

**Keywords:** methane reforming, chemical looping, core-shell, redox catalyst, perovskite, mixed ionic-electronic conductor, reaction mechanism, transient pulse injection

## Introduction

The recent increase in shale gas production from unconventional reservoirs has spurred renewed interest in natural gas conversion and methane valorization.<sup>1-3</sup> At present, most commercial methane conversion processes adopt an indirect approach due to its demonstrated reliability and high product yield.<sup>4-6</sup> In such processes, methane is converted into syngas (a mixture of carbon monoxide and hydrogen) in a reforming step in the presence of a gaseous reactant such as steam (steam reforming, Reaction 1), carbon dioxide (dry reforming, Reaction 2), and/or oxygen (partial oxidation, Reaction 3). The syngas is further processed to value-added products such as chemical feed stocks or liquid fuels. Despite their relatively high yield compared to direct methane conversion processes such as methane coupling,<sup>7,8</sup> the overall efficiency of indirect methane conversion processes is limited due to the energy-intensive nature of the gaseous oxidant generation and/or methane reforming steps.<sup>4,9</sup>



Among the above-mentioned reactions, the partial oxidation (POx) based reforming approach offers the ability to produce Fischer-Tropsch ready syngas. In addition, the overall reaction is exothermic, eliminating the need for heat transfer to the catalyst bed. At present, most POx reactions are performed in the presence of a heterogeneous catalyst. Among the reforming catalysts investigated to date,<sup>10-13</sup> transition metals such as Ni<sup>10,14-17</sup> and Co<sup>18-21</sup> and noble metals such as Pt, Pd, Rh, Ru, and Ir<sup>22-27</sup> are proven to be active for POx. However, these catalysts face challenges such as low selectivity, deactivation, and carbon formation, or their application is hindered due to high cost. Among these,

nickel-based catalysts have attracted the most attention because of their high effectiveness and relatively low cost compared to platinum group metals.<sup>10,17,28-30</sup> Hu and Ruckenstein used a transient method to study the mechanism of methane oxidation in the presence of gaseous oxygen on Ni-based catalysts,<sup>31-39</sup> reporting that CO<sub>2</sub> is the dominant product in the presence of nickel oxide, while the presence of metallic Ni promotes partial oxidation to CO. It was also reported that the reaction mechanism shifts from an Eley-Rideal mechanism in the oxidized form to Langmuir-Hinshelwood in the reduced state. Combined CO<sub>2</sub> reforming and partial oxidation on NiO/MgO catalyst under similar conditions were also investigated.<sup>36</sup> Based on experimental evidences, it was concluded that oxidation of CH<sub>x</sub> (x=1-3) controls conversion, while CO selectivity depends on the strength of oxygen bonds to the catalyst surface to the catalyst.<sup>32,39</sup> Although high CO selectivities and yields are reported for Ni-based catalysts, the high costs associated with cryogenic air separation still hinder the application of POx based methane reforming processes.

Compared to conventional reforming, the chemical looping strategy provides an alternative route for methane partial oxidation in absence of gaseous oxidants.<sup>10,11,40,41</sup> In the chemical looping reforming (CLR) scheme, lattice oxygen of an oxygen carrier is used to partially oxidize methane to syngas. The oxygen carrier is then regenerated in air. Since the oxygen carrier acts both as a catalyst (for syngas generation) and an oxygen donor (for methane oxidation), it is also referred to as a redox catalyst following a literature convention.<sup>42-44</sup> It is noted that such a redox catalyst is different from typical heterogeneous catalysts as it participates in the redox reactions both as a reactant and a catalyst. Besides eliminating the need of an energy-intensive air separation and/or steam generation unit, the CLR approach has the potential to reduce catalyst deactivation and increase CO selectivity by using appropriate combinations of oxygen carriers and supports as redox catalysts.<sup>45-47</sup> To date, many redox catalysts have been synthesized and tested under CLR conditions, most of which are composed of a

mixture of a primary metal oxide as an oxygen reservoir and an inert support to enhance the stability and activity of the redox catalyst.<sup>13,48–50</sup> Oxides of first-row transition metals, particularly nickel, are among the materials that received most attention because of their catalytic properties and high oxygen carrying capacity. Despite high selectivity of nickel-based redox catalysts toward syngas, their tendency toward coke formation under low oxygen partial pressures,<sup>51–53</sup> high cost, and environmental concerns<sup>54</sup> impose challenges in process and material design. Other transition metals such as Fe and Cu are tested as well, but compared to nickel, exhibited lower activity and/or selectivity.<sup>12,13</sup>

Perovskite materials are another class of materials that have been tested. Perovskites such as  $\text{La}_x\text{Sr}_{1-x}\text{FeO}_3$  (LSF) and  $\text{LaFeO}_3$  (LF) show up to 97% selectivity toward syngas formation.<sup>46,55,56</sup> However, these materials are often expensive due to the use of rare earth metals, and they suffer from low oxygen carrying capacity.<sup>12,57,58</sup> Our previous studies indicate that, by using an engineered structure of perovskite-coated metal oxide, the high oxygen capacity of transition metal oxides may be combined with high selectivity of perovskite surfaces to achieve high syngas selectivity while reducing coke formation and the cost of the redox catalyst.<sup>45,46</sup> Core-shell redox catalyst exhibited excellent activity, selectivity, and long term stability, showing no signs of deactivation after 100 cycles.<sup>45</sup> In contrast, unsupported iron oxide deactivate over few redox cycles.

Since the redox catalyst performance is crucial to the CLR process, a thorough understanding of the methane conversion mechanisms is necessary. The dynamic behavior of methane oxidation using an  $\text{Fe}_2\text{O}_3@\text{LSF}$  redox catalyst has been reported in our previous studies.<sup>46</sup> Results indicate that the methane oxidation scheme can be divided into 4 distinct regions: I) deep oxidation to  $\text{CO}_2$ , II) competing deep oxidation to  $\text{CO}_2$  and selective partial oxidation to CO, III) selective partial oxidation to CO with auto-activation, and IV) methane decomposition and coke formation. It is also suggested that the availability

and type of oxygen present on the catalyst surface determines the reaction mechanism. However, the mechanisms through which the methane oxidation reaction proceeds in each region and the corresponding rate-limiting steps are yet to be determined.

In this study, pulsed isotope exchange experiments are used to determine the methane oxidation pathways under different reaction regions. The dynamic nature of redox processes necessitates the use of such transient experiments. It is confirmed that the reaction mechanism experiences a significant change in the second region. While the overall reaction follows a modified Mars-van Krevlen mechanism throughout the reaction, methane conversion follows a reaction pathway that shifts from an Eley-Rideal type mechanism (in which methane weakly interacts with catalyst surface) to a Langmuir-Hinshelwood-like mechanism (in which methane strongly adsorbs and dissociates on the catalyst surface). Results suggest that the selectivity of syngas products is affected by the rate of oxygen conduction as well as availability and state of oxygen species on the surface of the redox catalyst.

## Experimental

### Catalyst synthesis

A detailed procedure for preparing the  $\text{Fe}_2\text{O}_3@\text{LSF}$  redox catalyst is reported elsewhere.<sup>45</sup> The catalyst is synthesized using a Pechini method.<sup>59</sup> A solution of stoichiometric amounts of  $\text{Fe}(\text{NO}_3)_3 \cdot 9\text{H}_2\text{O}$  (98%, Sigma Aldrich),  $\text{La}(\text{NO}_3)_3 \cdot x\text{H}_2\text{O}$  (99.9%, Sigma Aldrich),  $\text{Sr}(\text{NO}_3)_2$  (99%, Noah chemical) in deionized water is prepared and stirred at 30°C for 30 minutes; followed by the addition of citric acid (>99.5%, Sigma Aldrich) at a molar ratio of 2.5:1 between the acid and total cations in solution. Magnetic stirring at 50°C for 30 minutes forms a chelating solution. A second solution of a predetermined amount (1:1 molar ratio  $\text{Fe}_2\text{O}_3:\text{LSF}$ ) of suspended  $\text{Fe}_2\text{O}_3$  nanoparticles (<50nm, Sigma Aldrich) is concurrently prepared in a 60 vol% ethanol (reagent grade, Sigma Aldrich) water solution

under sonication. The suspension is allowed to settle for 6 hours, after which excess solvent is removed from the top layer of the solution. These two solutions (the nanoparticle suspension and the chelating solution) are combined and subjected to 30 minutes of vigorous stirring at 50°C. Gel formation is promoted with the addition of ethylene glycol (99%, Sigma Aldrich) in a 2:1 ratio to citric acid and subsequent stirring at 80°C for 2 hours. The resulting gel is kept at 400°C for 2 hours to evaporate volatile species, and annealed in air at 800°C for 4 hours. The morphology of the fresh and cycled particles are reported elsewhere.<sup>45</sup> In addition, previous studies have reported redox performance of pure iron oxide and/or perovskite based redox catalysts for methane oxidation.<sup>12,57,58,60–64</sup> Therefore, the current study focuses exclusively on probing the reaction pathways for the Fe<sub>2</sub>O<sub>3</sub>@LSF redox catalyst.

### **Pulse injection experiment**

Conventional steady-state methods provide little insight about the elementary steps that convert the reactants to products because these steps frequently proceed at comparable rates, which make them indistinguishable in a steady-state reaction. Furthermore, the dynamic nature of the redox catalysts makes them difficult to study using such steady-state methods. Pulse injection provides a very short residence time between the catalyst surface and methane, allowing the proposal or elimination of possible reaction pathways by combined injection of various reactants/isotopes under transient conditions. Figure 1 is a schematic representation of the experimental setup used to perform the pulse injection experiments.

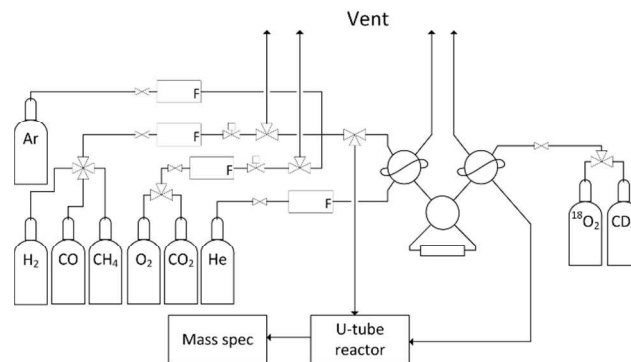


**Figure 1.** Schematic of the experimental setup used for pulse injection experiments.

Distribution and lag times of products were compared to a reference gas (Ar) at 700, 800, and 900°C in the three aforementioned regions: the oxidized state (region I, sample treated with 10 minute oxidation in 20% oxygen), the CO<sub>2</sub>/CO-reduced state (region II, sample treated with 15 minute reduction in 10% CO<sub>2</sub> and 10% CO), and the H<sub>2</sub>-reduced state (region III, sample treated with 15 minute reduction in 10% H<sub>2</sub>). These three pretreatment conditions have been confirmed to be effective to convert the fully oxidized redox catalysts into desired reaction regions through the examination of the phases and selectivity of the post-treatment redox catalyst. To investigate the behavior of the catalyst for methane oxidation in transient pulse injection mode, 300 pulses of 50% CH<sub>4</sub> (2.6 mL, balance Ar) were injected at each region with 1 minute loading and 1 minute injection time. The “loading time” refers to the duration in which the reactant gas mixtures are flowed into the sample loop to form a proper homogeneous mixture prior to injection. The “injection time” is referred to the duration that carrier gas (He) flowed through the sample loop to push the reactant gas pulse into the reactor. To study the effect of relaxation time (the time between two consecutive pulse injections) on the distribution of lattice oxygen and the resulting change in CO/CO<sub>2</sub> selectivity, an experiment similar to that outlined above was conducted in which 5 pulses of 50% methane (balance Ar) were injected at 15 second intervals (10 second injection, 5 second loading), and allowed 2.5 minutes relaxation time followed by a single 50%

methane pulse at 700, 800, and 900°C. The reactor effluent was analyzed to determine the effect of relaxation time upon product distributions or the overall activity of the catalyst.

Isotope experiments were conducted in each of the aforementioned regions using CD<sub>4</sub> (Sigma Aldrich, 99% purity) and <sup>18</sup>O<sub>2</sub> (Sigma Aldrich, 99% purity) at 700, 800, and 900°C. Pulses of 25% CH<sub>4</sub> and 25% CD<sub>4</sub> (1 mL, balance Ar) were introduced with 30 second loading and 30 second injection times, and the effluent was monitored for CH<sub>4</sub>, CH<sub>3</sub>D, CH<sub>2</sub>D<sub>2</sub>, CHD<sub>3</sub>, CO, and CO<sub>2</sub> in order to determine the amounts of methane reacted and exchanged. Pulses of <sup>18</sup>O<sub>2</sub> were similarly introduced over the sample pre-oxidized in <sup>16</sup>O<sub>2</sub>, monitoring the effluent for <sup>18</sup>O<sub>2</sub>, <sup>18</sup>O<sup>16</sup>O, and <sup>16</sup>O<sub>2</sub>. Finally, 0.2 mL pulses of <sup>18</sup>O<sub>2</sub> (1mL, balance Ar) were injected while injecting a broadened pulse of CH<sub>4</sub> (broadened by sending a 5 mL injection through a 150 mL broadening tube), and the distribution of carbonaceous products (C<sup>16</sup>O, C<sup>18</sup>O, C<sup>16</sup>O<sub>2</sub>, C<sup>16</sup>O<sup>18</sup>O, C<sup>18</sup>O<sub>2</sub>), isotopic hydrogen (HD, D<sub>2</sub>) and water isotopes (HDO, D<sub>2</sub>O) were recorded. These isotope studies provided quantitative information regarding the activity of the catalyst surface towards oxygen and methane disassociation at 700, 800, and 900°C.

## Results and discussion

Our previous studies indicate that the Fe<sub>2</sub>O<sub>3</sub>@LSF redox catalyst at 900 °C undergoes 3 reaction regions prior to near-depletion of active lattice oxygen, which is marked by the onset of coke formation (region IV). The oxygen carrying capacity of the redox catalyst, defined as sample weight loss within the first three reaction regions, amounts to 13 w.t.%. Such a weight loss resulted mainly from the reduction of iron oxide to metallic iron. Oxygen defect formation in perovskite structure also contributed to the overall oxygen carrying capacity albeit at a lesser extent.<sup>46</sup> Figure 2a shows the reduction pattern of the redox catalyst in a fixed bed reactor at 900°C and 10% methane (balance Ar). The region transitions are marked by products shift toward CO due to the change in availability of active lattice

oxygen and the nature of the active surface sites. Figure 2b compares the selectivity of CO and CO<sub>2</sub> in the first 3 regions. It is evident that the redox catalyst undergoes a mechanism change that causes significant selectivity variations. Very similar pattern and product selectivity is observed at a methane concentration of 5%.

To obtain a better understanding of the underlying mechanisms causing such selectivity shifts, transient experiments are conducted on the core-shell redox catalyst. To ensure that the pulse injection mode is representative of the continuous methane oxidation experiment, a long term pulse injection run (300 pulses) was performed. The resulting methane oxidation pattern (Figure S1) and selectivity (Table S1) were compared with those of continuous oxidation and a very good agreement is observed, especially in the first and third regions. This experiment also confirms that the size of the pulse is small enough such that the surface and bulk property of the redox catalyst is not significantly altered within a single pulse (with the exception of the first pulse in region I). In this study, emphasis is placed on the first and the third regions, as the observed behaviors indicate distinct mechanisms in these two regions. From a practical standpoint, it is desirable to minimize region I and promote region III to enhance syngas selectivity.

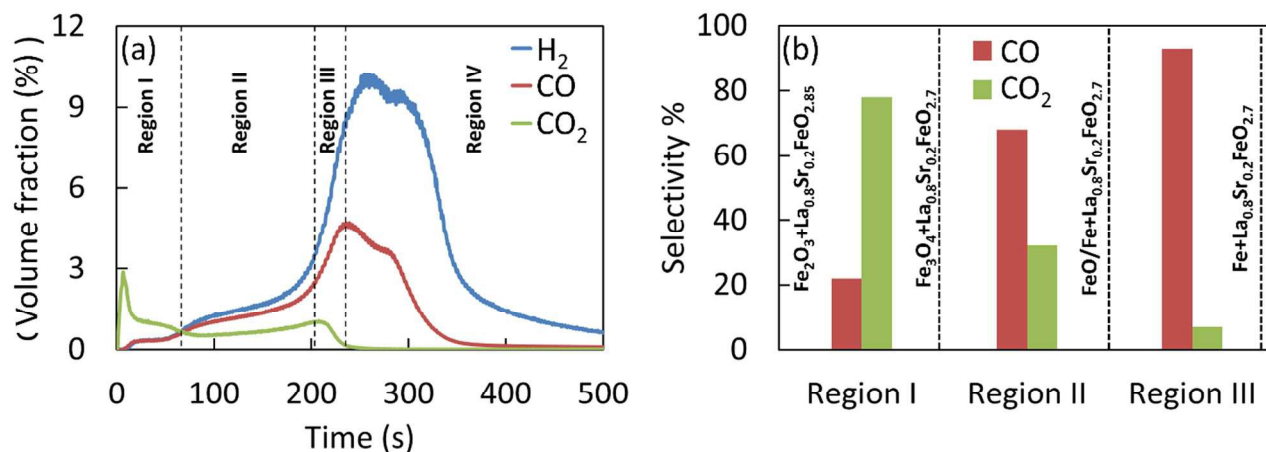


**Figure 2.** (a) Product evolution from the oxidation of methane on  $\text{FeO}_x\text{@LSF}$  core-shell redox catalyst, (b) Average selectivity of CO and  $\text{CO}_2$  in the first 3 regions for methane reduction at  $900^\circ\text{C}$  in 10 Vol. % methane (balance Ar).

Our previous studies indicate that reaction region transitions generally correspond to the oxidation state change of iron oxide in the redox catalyst<sup>46</sup> (Figure 2b): transition from region I to region II corresponds to a phase change from  $\text{Fe}_2\text{O}_3/\text{Fe}_3\text{O}_4$  to  $\text{Fe}_3\text{O}_4/\text{FeO}$  whereas region II to region III approximately resembles the partial reduction of wüstite phase to metallic iron. The onset of region IV is consistent with complete reduction of the wüstite ( $\text{FeO}$ ) phase to metallic iron. To confirm that the sample pretreatment procedures presented in the experimental section convert the catalyst to the desired regions, XRD is performed (Figure 3a). XRD patterns confirmed formation of  $\text{Fe}_2\text{O}_3$ ,  $\text{FeO}$ , and  $\text{Fe}$  after treatment in  $\text{O}_2$ ,  $\text{CO}+\text{CO}_2$ , and  $\text{H}_2$  respectively. The LSF phase is stable under all three treatment conditions. Figure 3b compares the average selectivity of CO and  $\text{CO}_2$  during injection of 5 pulses after each pretreatment. The pulse injection selectivity data shows very good consistency with the average selectivities at 3 corresponding regions (Figure 2b) which further confirms that the pretreatments convert the catalyst to the desired reaction regions.

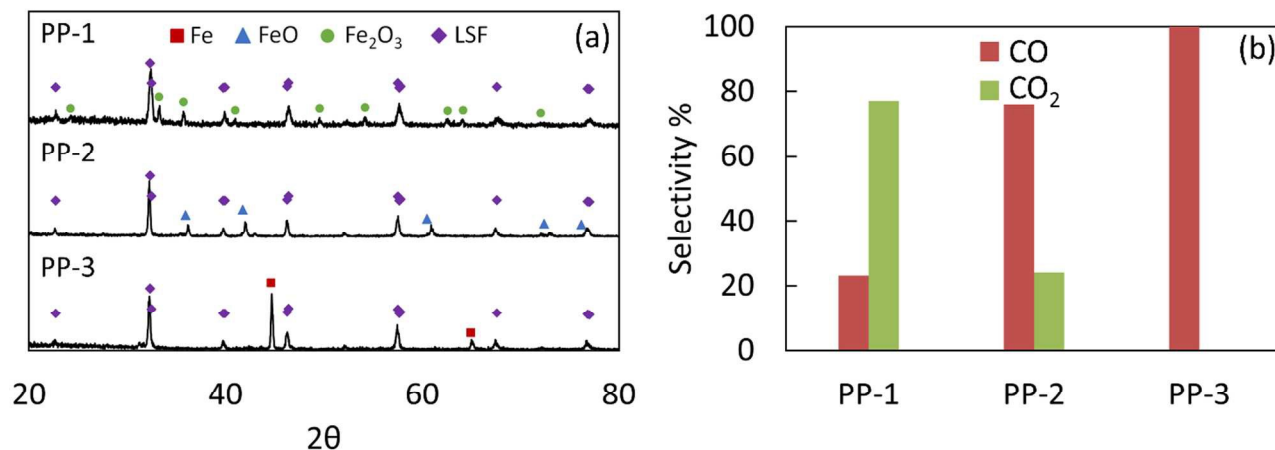


**Figure 3.** (a) XRD pattern and assigned phases after the three pretreatment procedures (PP): PP-1, oxidation in 10% oxygen for 10 mins, PP-2, CO/CO<sub>2</sub>... to obtain samples representing the first three regions, respectively; (b) Average selectivity of CO and CO<sub>2</sub> during 5 pulse injections after each pretreatment at 900°C (50 Vol. % methane, balance Ar)

### Deep oxidation region (region I)

Chemisorbed and surface oxygen species are generally considered to be responsible for deep methane oxidation.<sup>46</sup> Therefore, one would anticipate low CO selectivity in the first few pulse injections on oxidized redox catalysts. This is confirmed in the first four pulse injections. After the fourth pulse, selectivity of CO started to increase, and the catalyst transitioned to the second region (Figure 4). The following experiments are designed to probe the amount and nature of the non-selective surface oxygen species, through: i) examination of product responses in consecutive pulses; ii) increasing the bulk lattice oxygen supply (increasing the relaxation time); iii) co-feeding gaseous oxygen and monitoring its effects on product distribution and rates of reactions.

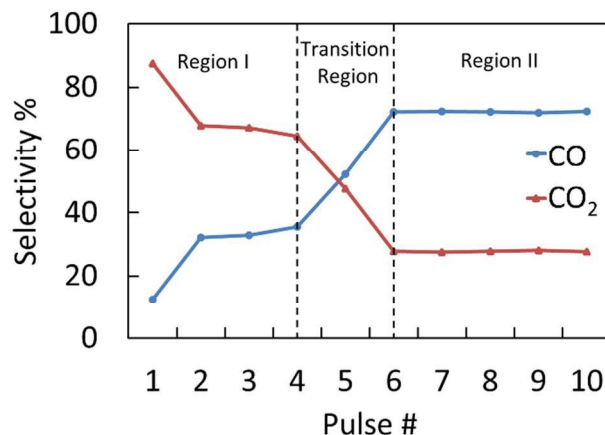


**Figure 4.** Selectivity transition from CO<sub>2</sub> to CO within the first 10 pulse injections.

During pulse experiments, the pattern and time scale at which different products exit from the reactor can provide indications of reaction pathways and primary/secondary products for each region. Figure 5 illustrates the responses of H<sub>2</sub>, CH<sub>4</sub>, CO, and CO<sub>2</sub> (normalized by the sum of all carbonaceous species) relative to an internal standard (Ar) in the first pulse at 900°C and Figure 5b compares the CO and CO<sub>2</sub> responses in the first and the second pulse. The behaviors of pulses 3 and 4 are very similar to that of the second pulse. It is noted that CO<sub>2</sub> in the first pulse peaks ~0.5 seconds earlier than the internal standard although unreacted methane reaches its maximum slightly later than the argon standard. The fact that CO<sub>2</sub> peak appears significantly earlier than unconverted methane indicates that deep methane oxidation is primarily resulted from the nonselective, electrophilic surface oxygen species, which is facile in both abstraction of the first H atom from CH<sub>4</sub> and non-selective combustion reactions.<sup>65,66</sup> Such surface oxygen species is abundant on the fresh, fully oxidized oxygen carrier but can be quickly consumed during the first pulse. While such surface oxygen species can be replenished by evolution of lattice and chemisorbed oxygen in lattice oxygen vacancies: ( $O^{2-} \leftrightarrow O^- \leftrightarrow O_2^{2-} \leftrightarrow O_2^-$ ), the rate of replenishment is significantly slower than the rate of oxygen removal by CH<sub>4</sub>/CO/H<sub>2</sub> (see Figure 6). The lack of surface oxygen species for methane deep oxidation causes the CO<sub>2</sub> signal to decay 0.6 seconds

before the peaking of methane supply. The slow evolution of lattice and chemisorbed oxygen species to the surface oxygen species is confirmed by the long  $\text{CO}_2$  tail in the first pulse. Another evidence of slow oxygen evolution is the re-appearance of  $\text{CO}_2$  peaks in the subsequent pulses at a significantly smaller scale (Figure 5b) and its dependence on relaxation time (Figure 6), as will be discussed in the next section. It is also noted that carbon monoxide and hydrogen started to form after the peaking of  $\text{CO}_2$  during the first pulse (Figure 5a). This again confirms the non-selective nature of surface oxygen species. As illustrated in Figure 5b, this delay was not observed in any of the subsequent pulses.

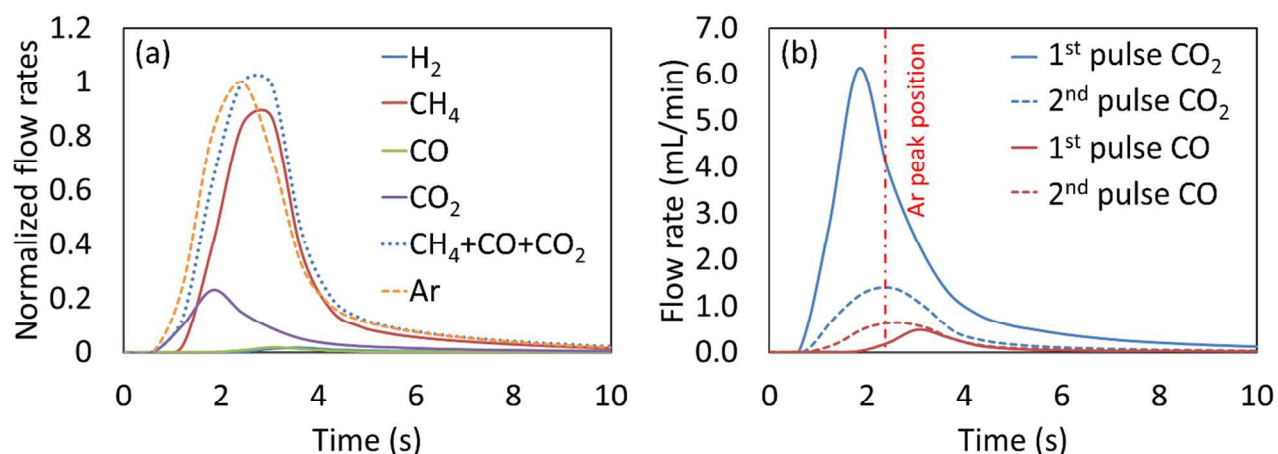


**Figure 5.** Normalized responses of products to injection of 2.6 mL methane (50%) at 900°C in (a) first pulse injection ( $\text{CH}_4$ ,  $\text{CO}$ ,  $\text{CO}_2$ , and  $\text{H}_2$  are normalized by the sum of all carbonaceous species and Ar is normalized to show a comparable scale as total carbonaceous species) and (b) Comparison of the intensity and position of  $\text{CO}$  and  $\text{CO}_2$  responses during first and second pulse injections.

With the exception of the first pulse, methane conversion rate in region I is significantly lower than that in region III (Figure 2a). The fact that  $\text{CO}_2$ , which is the main product in this region, formed without delay compared to methane pulse suggests that methane dissociation and product desorption steps are not rate-limiting in this region. An alternative explanation for the slow methane oxidation kinetics includes low surface coverage of active oxygen species which serve as active sites for dissociative

adsorption of methane. The availability of such surface oxygen species, as discussed earlier, can be limited by oxygen conduction and evolution after pulse 1. To probe the effect of lattice oxygen conduction, a redox catalyst sample is exposed to consecutive pulses of methane with varying relaxation times. Provided that oxygen conduction from the oxide lattice is a rate limiting step, longer relaxation time should allow increased amounts of bulk lattice oxygen being conducted to the surface and evolve into active oxygen species. This can, in turn, lead to increased methane conversion and decreased CO selectivity. As shown in Figure 6, selectivity of CO increased from 4.55% to 13.83% during the injection of 5 pulses with 15 seconds relaxation time; however, resting the sample for 2.5 minutes caused the selectivity to go down to 11.62%. The overall methane conversion also reduced from 43.7  $\mu\text{L}$  in the first pulse to 22.2  $\mu\text{L}$  in the fifth pulse and increased back up to 24.6  $\mu\text{L}$  after longer relaxation. This indicates that oxygen conduction is indeed rate-limiting in this region at 900°C and surface oxygen species are crucial for methane activation and oxidation. Similar experiments are also performed at lower temperatures (700 and 800°C), and no considerable selectivity toward CO is observed regardless of the relaxation time.

To probe the role of methane adsorption/dissociation in region I, methane isotope exchange experiments are conducted through co-injection of  $\text{CH}_4$  and  $\text{CD}_4$ . As can be seen in Figure 7a, a very small amount of exchanged products are observed in the effluent gas at 900°C. Reducing the temperature to 800°C lowered the amount of exchange (Figure 7b). This indicates i) low surface coverage of activated methane species and/or ii) facile oxidation of such species to  $\text{CO}_x$  products. Since the rate determining step is the oxidation reaction, which is controlled by oxygen conduction (methane dissociation and product desorption are not rate limiting from pulse experiments), the density of active sites for methane dissociation is concluded to be low. Moreover, such active sites are likely to be provided by surface oxygen species, which is affected by the rate of lattice oxygen conduction and

evolution. Assuming a homogeneous dissociation of CH<sub>4</sub>/CD<sub>4</sub>, the rate of CH<sub>4</sub> dissociation is 1.67 times faster than that of CD<sub>4</sub> at 900°C due to a kinetic isotope effect.<sup>38</sup> However, the observed difference between the amount of CH<sub>4</sub> and CD<sub>4</sub> exchanged does not agree with the calculated ratio as CD<sub>4</sub> showed higher amount of conversion and exchange. This further confirms that C-H bond cleavage is not the rate limiting step.

Isotope exchange experiments for <sup>16</sup>O<sub>2</sub> and <sup>18</sup>O<sub>2</sub> are also performed to determine the relative importance of oxygen evolution and bulk O<sup>2-</sup> conduction. The isotope exchange experiment (Figure 8) confirmed that the surface of the catalyst in this region is highly active for oxygen dissociation and exchange. Within a short pulse, 0.014 mmol <sup>18</sup>O atoms are exchanged with <sup>16</sup>O from either gaseous oxygen molecule or lattice oxygen in the catalyst. This corresponds to an average exchange rate of 2.32×10<sup>-5</sup> mmol/s per gram of catalyst and is at least 7.7 times of the surface oxygen considering the relatively low surface area of the cycled sample (4.1 m<sup>2</sup>/g) and assuming the exposure of the oxygen rich (002) crystallographic plane of LSF. The amount of exchanged oxygen atoms also corresponds to ~78% of the total isotope oxygen atoms (<sup>18</sup>O) injected and ~4.6% of the total lattice oxygen available. The significant amount of <sup>18</sup>O exchanged with lattice oxygen (<sup>16</sup>O<sup>2-</sup>) indicates that oxygen evolution (O<sub>2</sub> ↔ O<sub>2</sub><sup>-</sup> ↔ O<sub>2</sub><sup>2-</sup> ↔ O<sup>-</sup> ↔ O<sup>2-</sup>) is highly facile. The high exchange rate may suggest distinct oxygen adsorption/incorporation and desorption sites on the catalyst surface, with incorporation of dissociated oxygen species at the adsorption sites promoting the diffusion of surface or bulk lattice oxygen to the desorption sites. This observation is similar to the bismuth molybdate re-oxidation mechanism suggested previously.<sup>44,67</sup> In absence of gaseous oxygen, however, replenishment of oxygen on the surface can only be achieved through lattice oxygen conduction from the bulk under a modified Mars-van Krevelen mechanism.

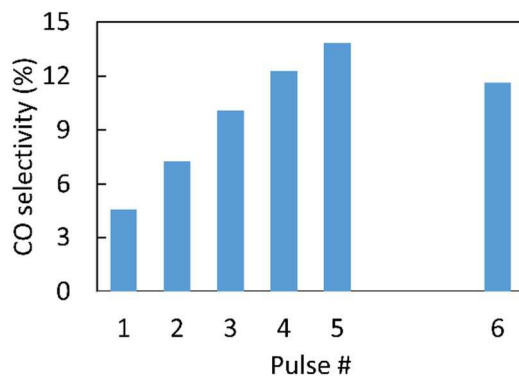


**Figure 6.** Effect of relaxation time on CO selectivity in the first region at 900°C (pulse 1-5 has a relation time of 15 seconds whereas pulses 5-6 has a longer relaxation time of 150 seconds).

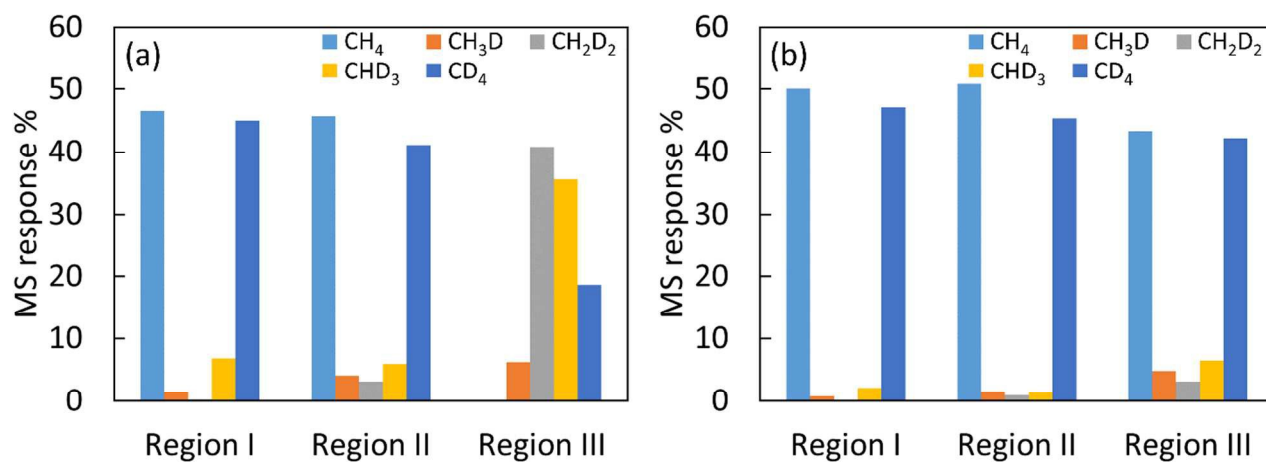


**Figure 7.** Relative distribution of products in methane isotope exchange experiments on the catalyst surface at (a) 900°C and (b) 800°C.

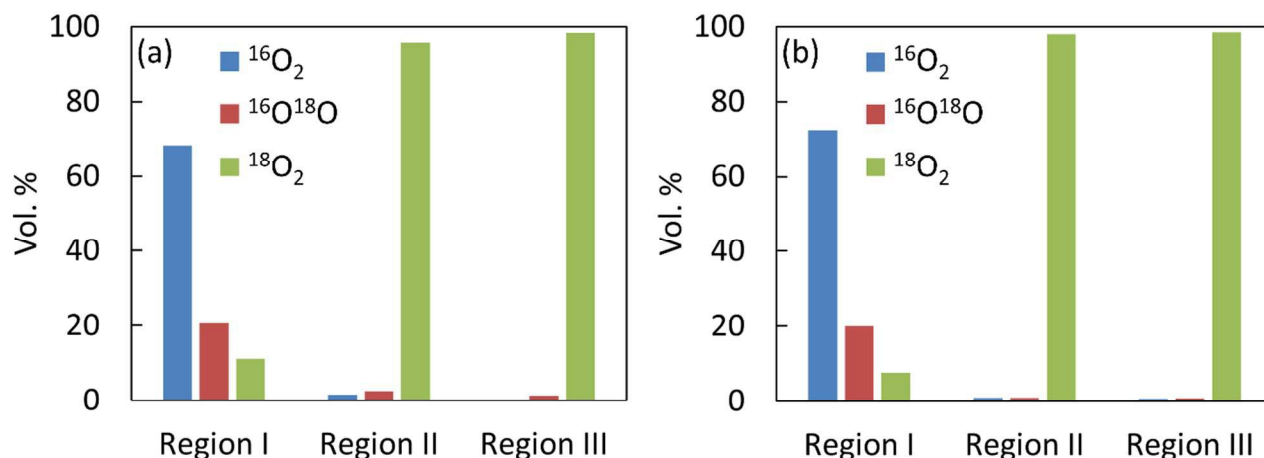


**Figure 8.** Relative distribution of products in oxygen isotope exchange experiments on the catalyst surface at (a) 900°C and (b) 800°C (the volume percents are normalized to the total oxygen in the outlet stream).

To further confirm the methane conversion mechanism in Region 1, a 1 mL pulse of 20%  $^{18}\text{O}_2$  (balance Ar) is injected to the redox catalyst during a broadened 5 mL pulse of methane (Figure 9a). The  $^{18}\text{O}_2$  injection caused over 70% increase in methane conversion and a decrease in CO selectivity. The injection of isotopic oxygen did not noticeably affect the formation of carbon monoxide; rather, the additional methane converted is mostly converted to  $\text{CO}_2$ . The instantaneous selectivity of  $\text{CO}_2$  increased from 74.25% to 84.36% during  $^{18}\text{O}_2$  injection. The enhancement of methane conversion with  $\text{O}_2$  injection again indicates that supply of surface oxygen species determines the overall reaction rate and such oxygen species are responsible for deep oxidation of methane. Another observation from this experiment is that a majority of the  $\text{CO}_2$  produced with  $^{18}\text{O}_2$  injection does not contain  $^{18}\text{O}$ . Further investigation indicates that this is largely resulted from surface oxygen exchange between bulk lattice oxygen and  $\text{CO}_2$  products (see supplemental file, Figure S3). It was also observed that  $\text{C}^{18}\text{O}^{16}\text{O}$  represents a significantly higher portion of  $\text{CO}_2$  produced at a higher space velocity (Figure 9b). This indicates that  $\text{C}^{18}\text{O}^{16}\text{O}$  is one of the primary products from methane oxidation after  $^{18}\text{O}_2$  injection. This once again confirms the participation of active surface oxygen species for methane activation in region I.

This abovementioned experimental evidence indicates that, in region I, oxygen evolution follows a modified Mars-van Krevelen mechanism, i.e., surface oxygen consumed for methane activation and oxidation is replenished by lattice oxygen conducted from the bulk. The overall rate of methane conversion is determined by the bulk oxygen conduction rate, i.e., although the surface is quite active for oxygen evolution and exchange in the presence of gaseous oxygen, the supply of active lattice oxygen from the bulk is rate-limiting when molecular oxygen is absent. In addition, although dissociative adsorption of methane is likely to occur in the presence of electrophilic surface oxygen species such as  $O^-$ , the interaction between methane and the catalyst surface is weak. Therefore, methane conversion can be approximated by the Eley-Rideal mechanism.

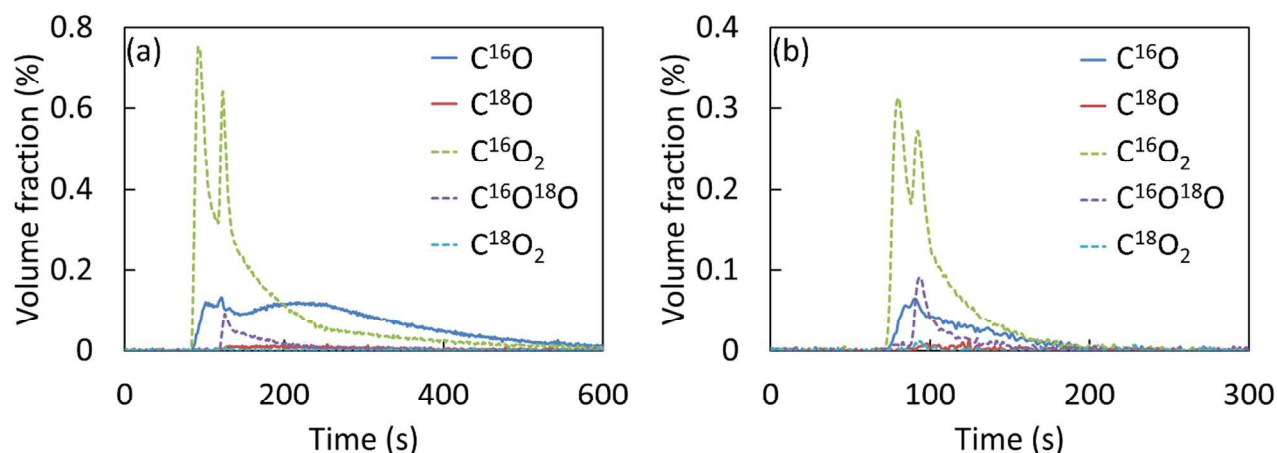


**Figure 9.** Response to a broadened pulse of methane combined with a sharp pulse of  $^{18}O_2$  at  $900^\circ C$  in the first region at (a) 50 and (b) 150 mL/min total gas flow rate.

### Selective oxidation region (region III)

The third region in the reduction scheme is defined as the region in which activity of the redox catalyst significantly increased and the reaction mechanism shifted predominantly towards selective

oxidation of methane to CO. The formation of active metallic sites, coupled with slightly lower diffusive oxygen flux (due to a lower oxygen gradient within the catalyst), is likely to be responsible for higher selectivity and increasing activity. A set of experiments similar to those discussed in the previous section are conducted to develop a better understanding of the reaction pathways in the third region. Analysis of the product responses when injecting a pulse of methane in this region shows that both H<sub>2</sub> and CO hit their maximum concentrations with ~1 second delay compared to the internal standard. Hydrogen showed relatively the same tail length when compared to the oxidized region, while the CO tail showed about 2 seconds delay (Figure 10b). Analyzing the selectivity of catalyst toward CO with different relaxation times confirms that the methane conversion rate in Region 3 is also controlled by oxygen conduction (Figure 11). While injection of 5 pulses at short (15 seconds) intervals increased selectivity, a noticeable selectivity drop is observed after resting the catalyst for a longer duration (2.5 min).

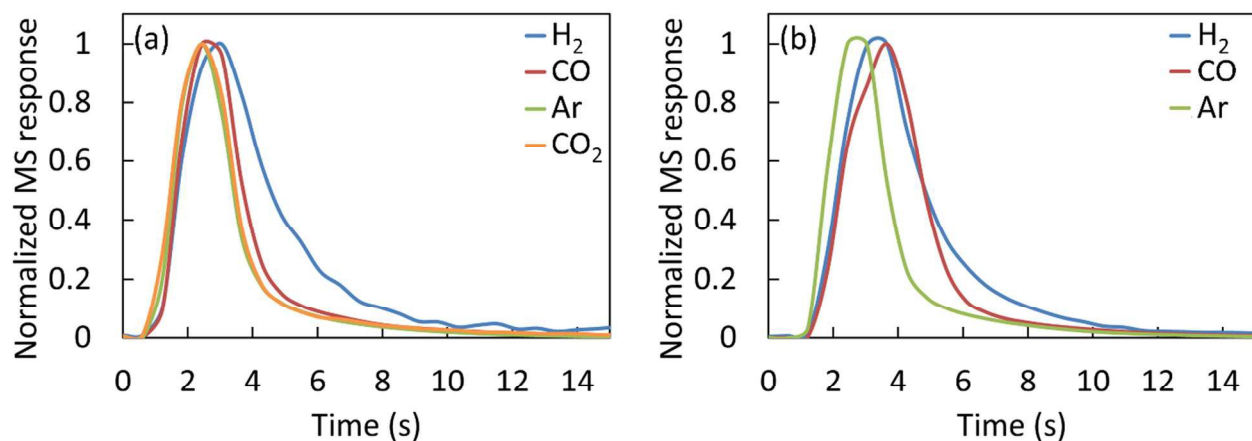


**Figure 10.** Normalized responses of products to injection of 1 mL methane (50%) at 900°C in (a) second region and (b) third region.

Figure 7 shows the relative concentrations of CH<sub>4</sub>, CD<sub>4</sub>, and exchanged methane. Over 80% of the unreacted CH<sub>4</sub> and CD<sub>4</sub> exited the reactor as CH<sub>3</sub>D, CH<sub>2</sub>D<sub>2</sub>, and CHD<sub>3</sub>. This is conclusive evidence that methane dissociation in this region is significantly faster than its conversion, and that availability of

surface oxygen controls the overall reaction rate. This also suggests that while oxygen evolution still maintains modified Mars-van Krevelen reaction mechanism behavior, methane conversion shifts toward a Langmuir-Hinshelwood type mechanism in which methane dissociates and the active surface species reacts with oxygen species on the surface. It should be noted that in this region, no  $\text{CH}_4$  is observed in the effluent gas at  $900^\circ\text{C}$ . Hu et al. reported a similar phenomenon in methane exchange experiments on nickel catalyst.<sup>37</sup> This could potentially be attributed to the kinetic isotope effect, which makes  $\text{CH}_4$  dissociate and convert more easily. Reducing the temperature to  $800^\circ\text{C}$  lowered the amount of exchanged and converted methane by  $\sim 50\%$  and  $80\%$  respectively. At  $700^\circ\text{C}$ , no appreciable amount of conversion or exchange is observed in any of the regions.

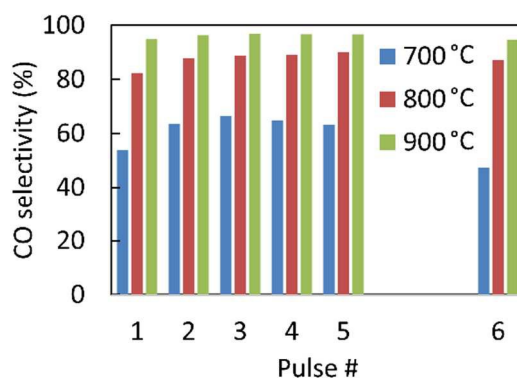


**Figure 11.** Effect of relaxation time on CO selectivity in the third region (pulse 1-5 has a relaxation time of 15 seconds whereas pulses 5-6 has a longer relaxation time of 150 seconds).

As expected, oxygen isotope experiments did not show  $^{16}\text{O}_2$  and  $^{16}\text{O}^{18}\text{O}$  in the products because most of the injected oxygen is incorporated into the oxygen-deficient lattice of the perovskite or simply oxidizes the iron cores. The trace amount of  $^{18}\text{O}_2$  observed is attributable to bypass from the catalyst. Injection of sharp pulses of  $^{18}\text{O}_2$  in a broadened methane pulse, as illustrated in Figure 12, leads to increased CO production. No  $\text{CO}_2$  is produced during this experiment and the selectivity of CO remained unchanged at nearly 100%. Such an observation confirms a number of mechanistic insights.

Firstly, surface oxygen species cannot be responsible for methane activation in region III. Rather, metallic-like sites on the reduced surface are likely to be responsible for methane dissociation in this region. This is further confirmed by TPD-DRIFTS (Temperature Programmed Desorption – Diffuse Reflectance Infrared Fourier Transform Spectroscopy) results (Figure S4). While oxidized catalysts show no CO chemisorption capacity, reduced catalyst exhibited noticeable CO chemisorption and activation capability, which is characteristic of metallic active sites. As one would anticipate, due to the significant oxygen deficiency in the surface and bulk of the catalyst, only a very small fraction of injected oxygen can evolve into the non-selective surface oxygen species near the metallic-like methane dissociation sites. Secondly, oxygen supply from the bulk still control the methane conversion rate in Region 3, even though the active surface sites have transitioned from surface electrophilic oxygen species to metallic surface centers; Thirdly, the gaseous oxygen incorporated into the surface are of ionic ( $O^{2-}$ ) nature. Comparison of  $C^{18}O$  selectivity versus  $C^{16}O$  at different space velocities in Figure 12 indicates that  $C^{18}O$  is a primary product after  $^{18}O_2$  injection and a significant portion of the additional  $C^{16}O$  is likely to form through subsequent oxygen exchange. It should also be noted that injection of the broadened methane pulse in region III pushed the catalyst to the forth region as  $H_2:CO$  ratio is higher than 2 due to methane decomposition.

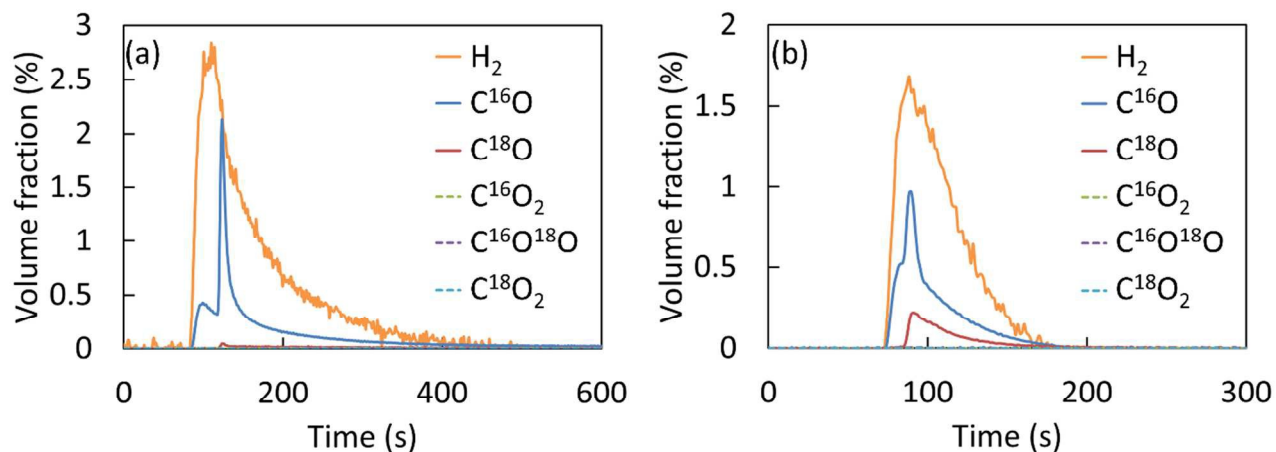


**Figure 12.** Response to a broadened pulse of methane combined with a sharp pulse of  $^{18}\text{O}_2$  at  $900^\circ\text{C}$  in the third region at (a) 50 and (b) 150 mL/min total flow rate.

### Competing deep and selective oxidation region (region II)

In the second region, a combination of the two reaction pathways occurs. As the redox catalyst is gradually reduced, more metallic-like surface sites are exposed, thereby shifting the selectivity toward CO. The time scale of the product responses in this region (Figure 10a) is relatively similar to the pattern observed in the later part of the first region but CO selectivity slowly increased as the catalyst becomes more reduced. Additional experimental data are summarized in the supplemental document.

Isotope exchange experiments showed some degree of exchange between methane and  $\text{CD}_4$ , but the amount of exchange was significantly smaller compared to the third region (Figure 7a). Like the third region, the second region also showed a lower amount of exchange and conversion at lower temperatures (Figure 7b). Oxygen isotope exchange did not show any sign of exchanged products as the injected oxygen either filled in the oxygen vacancies in the perovskite lattice and/or oxidized the metal core, or bypassed the catalyst bed.

Based on the above-mentioned experimental evidence, it is concluded that methane activation and oxidation follows distinct mechanisms over the oxidized (region I) and reduced (region III) surfaces. Abundance of surface oxygen species in the first region, which accounts for deep oxidation, makes the formation of oxygenated surface species dominant; whereas the lack of surface oxygen on the oxygen-deprived surface allows methane activation on metallic sites on the surface. The resulting  $\text{CH}_x$  species will then react with lattice oxygen conducted from the iron oxide core to form partial oxidation products. This is consistent with our methane TPR data (Figure S2) as it showed methane conversion products shifts from  $\text{CO}_2$  and  $\text{H}_2\text{O}$  (deep oxidation by loose, surface oxygen species) at lower temperatures to  $\text{CO}$  and  $\text{H}_2$  (partial oxidation by lattice oxygen) at higher temperatures. Although C-H bond in methane is rather stable, availability of active sites on the redox catalyst coupled with high reaction temperature allows relatively effective methane activation in all three reaction regions of interest. Figure 14 schematically illustrates the mechanism change during the course of the metal oxide reduction reaction.

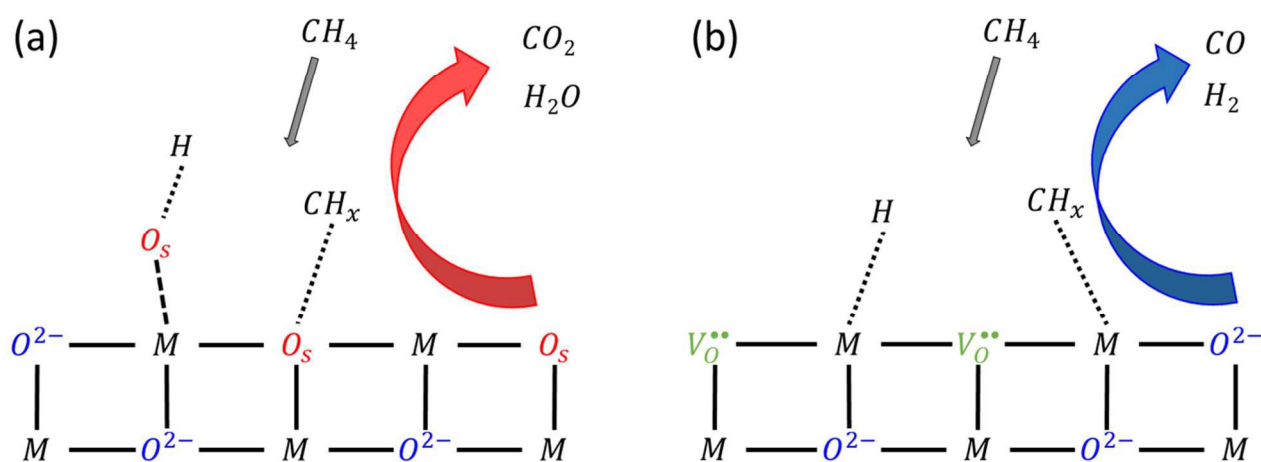


**Figure 13.** Schematics of methane activation and conversion of (a) oxidized and (b) reduced catalyst surface (M represents metal atoms).

## Conclusion

This article investigates the underlying mechanisms of methane partial oxidation over  $\text{Fe}_2\text{O}_3@\text{LSF}$  redox catalyst using a transient pulse injection method. The dynamic nature of reactions between methane and the redox catalyst introduces a four-region reduction scheme. In this study, a pulse injection system is used to inject sharp, transient pulses of various reactants in different sequences and concentrations to explore potential reaction pathways in different regions. The results indicate that the availability and nature of surface oxygen determines the reaction pathway and product selectivity. Oxygen anion conduction and/or its evolution to electrophilic surface oxygen species is determined to be the rate-limiting step in all the reduction regions of interest.  $\text{Fe}_2\text{O}_3@\text{LSF}$  redox catalyst goes through a mechanism change during the second region. While oxygen atoms maintain a modified Mars-van Krevelen mechanism throughout the reaction, the mechanism of methane conversion changes from the Eley-Rideal mechanism in the first region (in which methane is loosely adsorbed and reacts with electrophilic surface oxygen species) to a Langmuir-Hinshelwood-like mechanism in the third region (in which dissociatively adsorbed  $\text{CH}_x$  species are partially oxidized by  $\text{O}^{2-}$  species on the surface). These findings indicate that redox catalysts that can inhibit the formation of non-selective surface oxygen species while maintaining a steady supply of lattice oxygen to the catalyst surface can potentially lead to improved performance for methane partial oxidation.

## Acknowledgements

This work was supported by U.S. National Science Foundation (award no. CBET-1254351), Kenan Institute, and the Army research office DURIP Project under Award (65260-CH-RIP). The authors acknowledge the use of the Analytical Instrumentation Facility (AIF) at North Carolina State University, which is supported by the State of North Carolina and the National Science Foundation.

## References

- 1 M. R. Rahimpour, A. Mirvakili and K. Paymooni, *Energy*, 2011, **36**, 1223–1235.
- 2 B. Bao, M. M. El-Halwagi and N. O. Elbashir, *Fuel Process. Technol.*, 2010, **91**, 703–713.
- 3 J. A. Elia, R. C. Baliban, X. Xiao and C. A. Floudas, *Comput. Chem. Eng.*, 2011, **35**, 1399–1430.
- 4 J. R. Rostrup-Nielsen, *Catal. Today*, 2000, **63**, 159–164.
- 5 J. Eilers, S. A. Posthuma and S. T. Sie, *Catal. Lett.*, 1990, **7**, 253–269.
- 6 A. Y. Khodakov, W. Chu and P. Fongarland, *Chem. Rev.*, 2007, **107**, 1692–1744.
- 7 M. C. J. Bradford and M. A. Vannice, *Catal. Rev.*, 1999, **41**, 1–42.
- 8 D. Pakhare and J. Spivey, *Chem. Soc. Rev.*, 2014, **43**, 7813–7837.
- 9 D. J. Wilhelm, D. R. Simbeck, A. D. Karp and R. L. Dickenson, *Fuel Process. Technol.*, 2001, **71**, 139–148.
- 10 M. Rydén, A. Lyngfelt and T. Mattisson, *Fuel*, 2006, **85**, 1631–1641.
- 11 A. Thursfield, A. Murugan, R. Franca and I. S. Metcalfe, *Energy Environ. Sci.*, 2012, **5**, 7421–7459.
- 12 L.-S. Fan, *Chemical Looping Systems for Fossil Energy Conversions*, John Wiley & Sons, 2011.
- 13 J. Adanez, A. Abad, F. Garcia-Labiano, P. Gayan and L. F. de Diego, *Prog. Energy Combust. Sci.*, 2012, **38**, 215–282.
- 14 P. D. F. Vernon, M. L. H. Green, A. K. Cheetham and A. T. Ashcroft, *Catal. Lett.*, 1990, **6**, 181–186.
- 15 J. B. Claridge, M. L. H. Green, S. C. Tsang, A. P. E. York, A. T. Ashcroft and P. D. Battle, *Catal. Lett.*, 1993, **22**, 299–305.
- 16 Q. Miao, G. Xiong, S. Sheng, W. Cui, L. Xu and X. Guo, *Appl. Catal. Gen.*, 1997, **154**, 17–27.
- 17 L. F. de Diego, M. Ortiz, J. Adánez, F. García-Labiano, A. Abad and P. Gayán, *Chem. Eng. J.*, 2008, **144**, 289–298.
- 18 V. R. Choudhary, S. D. Sansare and A. S. Mamman, *Appl. Catal. Gen.*, 1992, **90**, L1–L5.
- 19 Y.-F. Chang and H. Heinemann, *Catal. Lett.*, 1993, **21**, 215–224.
- 20 E. Ruckenstein and H. Y. Wang, *Catal. Lett.*, 2001, **73**, 99–105.
- 21 H. Y. Wang and E. Ruckenstein, *Catal. Lett.*, 2001, **75**, 13–18.
- 22 L. Basini, A. Aragno and G. Vlaic, *Catal. Lett.*, 1996, **39**, 49–55.
- 23 F. van Looij, E. R. Stobbe and J. W. Geus, *Catal. Lett.*, 1998, **50**, 59–67.
- 24 Y. Boucouvalas, Z. Zhang and X. E. Verykios, *Catal. Lett.*, 1994, **27**, 131–142.
- 25 S. Tang, J. Lin and K. L. Tan, *Catal. Lett.*, 1998, **55**, 83–86.
- 26 N. Matsui, K. Nakagawa, N. Ikenaga and T. Suzuki, *J. Catal.*, 2000, **194**, 115–121.
- 27 D. A. Hickman and L. D. Schmidt, *J. Catal.*, 1992, **138**, 267–282.
- 28 M. Johansson, T. Mattisson, A. Lyngfelt and A. Abad, *Fuel*, 2008, **87**, 988–1001.
- 29 Z. Zhou, L. Han and G. M. Bollas, *Int. J. Hydrog. Energy*, 2014, **39**, 8535–8556.
- 30 J. Zhang and F. Li, *Appl. Catal. B Environ.*, 2015, **176–177**, 513–521.
- 31 Y. H. Hu and E. Ruckenstein, *Catal. Lett.*, 1995, **34**, 41–50.
- 32 E. Ruckenstein and Y. H. Hu, *Catal. Lett.*, 1995, **35**, 265–269.
- 33 Y. H. Hu and E. Ruckenstein, *J. Catal.*, 1996, **158**, 260–266.
- 34 Y. H. Hu and E. Ruckenstein, *J. Phys. Chem. B*, 1997, **101**, 7563–7565.
- 35 Y. H. Hu and E. Ruckenstein, *J. Phys. Chem. B*, 1998, **102**, 230–233.
- 36 E. Ruckenstein and Y. H. Hu, *Ind. Eng. Chem. Res.*, 1998, **37**, 1744–1747.
- 37 Y. H. Hu and E. Ruckenstein, *J. Phys. Chem. A*, 1998, **102**, 10568–10571.
- 38 Y. H. Hu and E. Ruckenstein, *Catal. Lett.*, 1999, **57**, 167–169.
- 39 Y. H. Hu and E. Ruckenstein, *Acc. Chem. Res.*, 2003, **36**, 791–797.

- 40 A. Lyngfelt, B. Leckner and T. Mattisson, *Chem. Eng. Sci.*, 2001, **56**, 3101–3113.
- 41 A. Murugan, A. Thursfield and I. S. Metcalfe, *Energy Environ. Sci.*, 2011, **4**, 4639–4649.
- 42 R. M. Contractor, D. I. Garnett, H. S. Horowitz, H. E. Bergna, G. S. Patience, J. T. Schwartz and G. M. Sisler, in *Studies in Surface Science and Catalysis*, ed. V. Cortés Corberán and S. Vic Bellón, Elsevier, 1994, vol. Volume 82, pp. 233–242.
- 43 M. P. House, A. F. Carley and M. Bowker, *J. Catal.*, 2007, **252**, 88–96.
- 44 R. K. Grasselli, *Top. Catal.*, 2002, **21**, 79–88.
- 45 A. Shafieifarhood, N. Galinsky, Y. Huang, Y. Chen and F. Li, *ChemCatChem*, 2014, **6**, 790–799.
- 46 L. M. Neal, A. Shafieifarhood and F. Li, *ACS Catal.*, 2014, **4**, 3560–3569.
- 47 L. Neal, A. Shafieifarhood and F. Li, *Appl. Energy*.
- 48 F. He, James A. Trainham, G. N. Parsons, J. Newman and F. Li, *Energy Environ. Sci.*
- 49 F. He and F. Li, *Energy Environ. Sci.*, 2015, **8**, 535–539.
- 50 N. L. Galinsky, A. Shafieifarhood, Y. Chen, L. Neal and F. Li, *Appl. Catal. B Environ.*, 2015, **164**, 371–379.
- 51 P. Cho, T. Mattisson and A. Lyngfelt, *Ind. Eng. Chem. Res.*, 2005, **44**, 668–676.
- 52 P. Gayán, L. F. de Diego, F. García-Labiano, J. Adánez, A. Abad and C. Dueso, *Fuel*, 2008, **87**, 2641–2650.
- 53 T. Mattisson, M. Johansson and A. Lyngfelt, *Fuel*, 2006, **85**, 736–747.
- 54 A. R. Oller, M. Costa and G. Oberdörster, *Toxicol. Appl. Pharmacol.*, 1997, **143**, 152–166.
- 55 O. Mihai, D. Chen and A. Holmen, *J. Catal.*, 2012, **293**, 175–185.
- 56 F. He, X. Li, K. Zhao, Z. Huang, G. Wei and H. Li, *Fuel*, 2013, **108**, 465–473.
- 57 Q. Imtiaz, D. Hosseini and C. R. Müller, *Energy Technol.*, 2013, **1**, 633–647.
- 58 F. Li and L.-S. Fan, *Energy Environ. Sci.*, 2008, **1**, 248–267.
- 59 S. Lee, H. S. Song, S. H. Hyun, J. Kim and J. Moon, *J. Power Sources*, 2010, **195**, 118–123.
- 60 J. E. Readman, A. Olafsen, Y. Larring and R. Blom, *J. Mater. Chem.*, 2005, **15**, 1931–1937.
- 61 J. G. McCarty and H. Wise, *Catal. Today*, 1990, **8**, 231–248.
- 62 Å. Slagtern and U. Olsbye, *Appl. Catal. Gen.*, 1994, **110**, 99–108.
- 63 H. X. Dai, C. F. Ng and C. T. Au, *J. Catal.*, 2000, **189**, 52–62.
- 64 X. P. Dai, Q. Wu, R. J. Li, C. C. Yu and Z. P. Hao, *J. Phys. Chem. B*, 2006, **110**, 25856–25862.
- 65 K. D. Campbell, H. Zhang and J. H. Lunsford, *J. Phys. Chem.*, 1988, **92**, 750–753.
- 66 Y. Jin, C. Sun and S. Su, *Phys. Chem. Chem. Phys.*, 2015, **17**, 16277–16284.
- 67 L. C. Glaeser, J. F. Brazdil, M. A. Hazle, M. Mehicic and R. K. Grasselli, *J. Chem. Soc. Faraday Trans. 1 Phys. Chem. Condens. Phases*, 1985, **81**, 2903–2912.

## Graphical abstract

Study on the mechanism of C-H bond activation and kinetic pathways of methane conversion using  $\text{FeO}_x@La_{0.8}Sr_{0.2}FeO_3$  redox catalyst

